Improved Decoupled Control of Modular Multilevel Converter under Constraint of Nearest Level Modulation via Disturbance Observer Design

Jaeyeon Park, Dongjoon Kim, Seungjun Lee, Graduate Student Member, IEEE, and Shenghui Cui, Member, IEEE

Abstract-Nearest level modulation (NLM) is an attractive modulation method for its implementation simplicity in modular multilevel converter (MMC). However, it introduces significant voltage and current distortion when the number of submodules (SMs) per arm is small, as in medium-voltage applications. While indirect modulation offers fully decoupled control of ac-side current, dc-side current and SM capacitor energy, its performance is fundamentally reliant on accurate arm voltage synthesis, making it incompatible with the large quantization error inherent in NLM. To resolve this conflict, this paper proposes a new control strategy based on a disturbance observer (DOB). The key idea is to estimate and actively compensate for the inevitable arm voltage synthesis error induced by NLM, thereby enabling fully decoupled control of indirect-modulated MMC even under NLM operation with a small number of SMs. A key advantage is its ease of implementation, as it requires no modifications to the conventional NLM and decoupled control structure. The validity and effectiveness of the proposed method in improving current quality and decoupled SM energy control are verified through both simulation and experimental results.

Index Terms—Disturbance Observer (DOB), Indirect Modulation, Modular Multilevel Converter (MMC), Nearest Level Modulation (NLM).

I. Introduction

ODULAR multilevel converter (MMC) has been highlighted as a scalable voltage-source converter (VSC) for high-power and high-voltage applications, such as high-voltage dc (HVDC) transmission system and medium-voltage dc (MVDC) distribution system, owing to its modularity and excellent quality of voltage and current waveforms [1]–[5].

In medium-voltage applications, such as MMC-based static synchronous compensator [6], [7] and motor drive [8], [9], where the number of submodules (SMs) in each arm is relatively small compared to HVDC applications, the carrier-based pulse-width modulation (PWM) scheme [10]–[13] is widely used to generate arm voltage following the given modulation reference, because it can minimize the quantization issue of arm voltage induced by the small number of SMs. However, this approach introduces two primary challenges: high switching losses due to the high-switching frequency operation of SMs, and increased control hardware complexity to generate synchronized and high-time resolution carrier signals for each SM [14].

Due to these challenges associated with PWM schemes, the nearest level modulation (NLM) scheme, also known

J. Park, D. Kim, S. Lee, and S. Cui are with the Department of Electrical and Computer Engineering, Seoul National University, Seoul 08826, Republic of Korea (e-mail: cuish@snu.ac.kr)

as nearest level control (NLC), which only determines the number of inserted SMs at each control period [15], is often considered a more feasible option when implementation simplicity and efficiency are prioritized. Especially MMC with a large number of SMs, such as those in HVDC applications, can effectively utilize NLM because the quantization issue of arm voltage is less pronounced with a sufficient number of levels. However, when the number of SMs is small, NLM scheme leads to a significant error in the arm voltage synthesis due to the rounding operation of the modulation reference to the nearest voltage level. This issue brings a significant challenge in practice to address as follows, since most vendors nowadays in industry are expanding business from HVDC applications to MVDC applications and not the other way around: The sophisticated controller system was developed and well established in orientation to HVDC applications, therefore the firmware is developed to be feasible only with NLM to reduce communication burdens. While developing a new controller system dedicated to MVDC applications enabling PWM functionality in the firmware not only calls for significant investment but also prolongs the delivery time.

To address this limitation of NLM in MMC with a small number of SMs, various NLM schemes have been proposed to increase the effective level of arm voltage and reduce the harmonic distortion of output voltage and current [16]-[19]. In [16], the rounding threshold of the NLM scheme is adjusted from 0.5 to 0.25 to increase the effective number of ac-side voltage levels. However, this method inherently modifies the average voltage of SM capacitor in steady state and does not suppress the circulating current. These issues are resolved in [17], by altering the small offset between the positive and negative value at double fundamental frequency. However, the method's performance is limited by its dependency on the acside power factor. Specifically, the initial phase of the offset must be adjusted according to the load, and consequently, effective circulating current suppression cannot be guaranteed across the entire range of power factors. In [18] and [19], the model predictive control approach is applied to the NLM scheme to satisfy multiple control objectives, such as reducing the distortion of output current and suppressing the circulating current. Although both methods show improved performance, they are not suitable for practical applications because of the lack of stability analysis for the control loop.

Focusing the way to generate modulation reference, there are two main approaches: direct modulation and indirect modulation (which is also known as compensated modulation) [20]. The direct modulation generates the modulation reference

based on the constant nominal SM capacitor voltage, while the indirect modulation generates it based on the instantaneously measured SM capacitor voltage [21]. Although the direct modulation inherently balances the SM capacitor voltage in steady state, it results in considerable second-order circulating currents which must be suppressed by extra passive [22], [23] or active [24] means. The dc-link voltage of the MMC is tightly coupled to the average SM capacitor voltage, and it results in considerable second-order oscillation voltages in the dc link in the case of ac-side single-line-to-ground (SLG) fault and can lead to malfunction of protection systems [25]. Moreover, direct modulation based control of MMC results in complicated impedance characteristics on the ac side in low frequency regions due to inherently incorrect arm voltage synthesis [26], [27], and it leads to instability issues due to interactions with ac grids. Such instability issue has been intensively reported in academia and industry in recent years [28], [29], and sophisticated harmonic state space analysis has to be employed to analyze the impedance characteristics of the MMC to enhance the stability [30]. On the other hand, the indirect modulation based decoupled control can inherently avoid second-order circulating currents, and dc-link voltage can be fully decoupled from the average SM capacitor voltage [21], [31], [32]. Therefore, inherently, no second-order oscillation voltage appears in the dc link in the case of a grid side SLG fault. Different from two-level converters or MMC under direct modulation based control, the dc-link current can be directly controlled [33]. Moreover, the impedance characteristics of the MMC on ac side becomes as simple as two-level converter due to accurate arm voltage synthesis, which significantly facilitates the impedance analysis to enhance the stability [34].

However, this decoupled control capability comes with a critical prerequisite. Since indirect modulation utilizes current control loops not only to control grid-side and dc-link currents but also to balance the SM capacitor energy, its performance fundamentally relies on the accurate synthesis of the arm voltage references. Consequently, this approach is typically considered effective only for MMCs that can ensure minimal voltage distortion, such as those employing PWM [31] or those with a sufficiently large number of SMs [14].

A common observation of the aforementioned improved NLM schemes [16]–[19] is that they are all developed based on the direct modulation approach. Therefore, they inherit its fundamental limitation described above. To the best of the authors' knowledge, there is no existing proper NLM scheme for indirect-modulated MMC with a small number of SMs that can fully decouple ac-side current control, dc-side current control, and SM capacitor energy balancing.

To address this research gap, this paper proposes a new control strategy for NLM operation of indirect-modulated MMC with a small number of SMs per arm. The key idea of the proposed method is employing a disturbance observer (DOB) to estimate and compensate for the arm voltage synthesis error induced by the rounding operation of NLM. A key advantage of the proposed method is that the DOB acts as an add-on component to the existing control structure, enabling the effective use of the well established controller system with a conventional NLM scheme and decoupled control

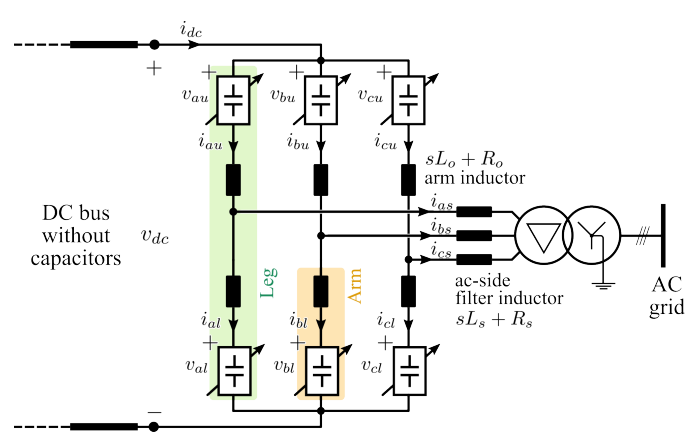


Fig. 1. Modular multilevel converter with ac grid and dc bus.

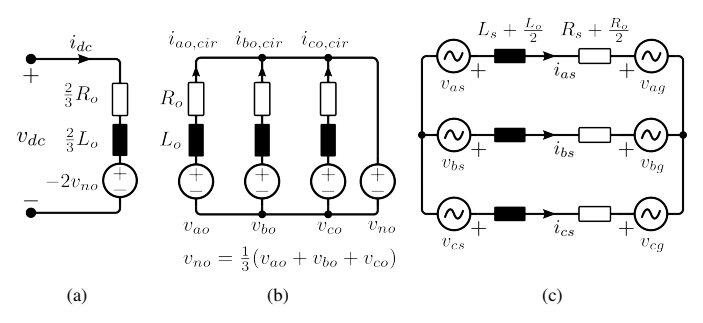


Fig. 2. Decoupled equivalent models of MMC. (a) dc-side current, (b) circulating current, (c) ac-side current. v_{xg} is the x-phase ac grid voltage.

structure without requiring any modifications to them. This characteristic significantly simplifies the implementation of the proposed method in practical applications.

The rest of the paper is organized as follows. Section II introduces the theoretical background of the proposed method, including the system model of MMC, overview of the decoupled control strategy and NLM operation for indirect-modulated MMC, and the principle of DOB. Section III analyzes the arm voltage synthesis error of NLM and presents the proposed control strategy. To ensure the stability of the overall system when the proposed method is integrated, a stability analysis is also provided. In Section IV and Section V, the effectiveness of the proposed method is validated through simulation and experimental results, respectively. Finally, Section VI concludes the paper.

II. THEORETICAL BACKGROUND

This section provides an overview of the modeling and decoupled control strategies for indirect-modulated MMC, which serve as the foundational control schemes in this study, following the approach in [32]. Since the proposed method, which is discussed in the following sections, is based on the DOB, this section also introduces the principle and stability conditions of DOB, as described in [35] and [36].

A. Decoupled Modeling and Control of MMC

Fig. 1 illustrates the schematic of MMC with ac grid and dc bus. i_{xu} , i_{xl} , and i_{xs} represent the x-phase current of upper arm, lower arm, and ac side, respectively. i_{dc} stands for the

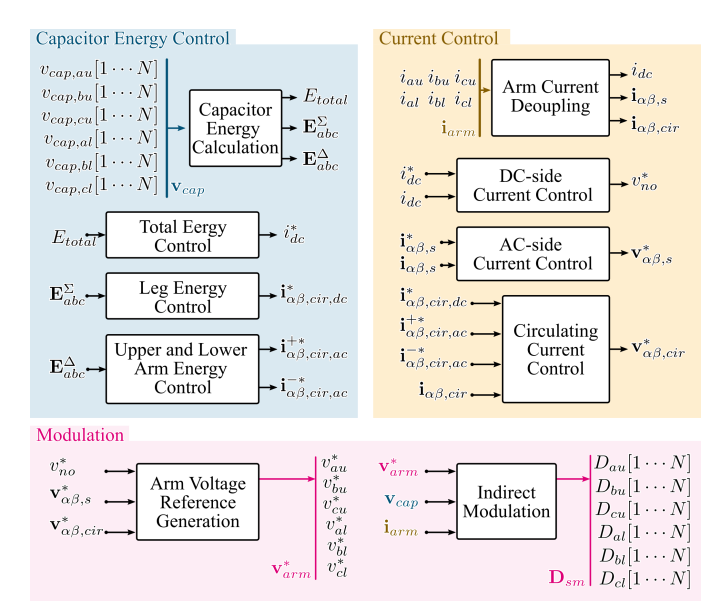


Fig. 3. Overview of the decoupled control strategy for inverter mode MMC. $\mathbf{E}_{abc}^{\Sigma}$ and $\mathbf{E}_{abc}^{\Delta}$ are defined as $\begin{bmatrix} E_a^{\Sigma} & E_b^{\Sigma} & E_c^{\Sigma} \end{bmatrix}^{\top}$ and $\begin{bmatrix} E_a^{\Delta} & E_b^{\Delta} & E_c^{\Delta} \end{bmatrix}^{\top}$, where E_x^{Σ} is the sum and E_x^{Δ} is the difference of the upper and lower arm capacitor energies for the x-phase leg. D_{xu} and D_{xl} are the duty cycles of the SMs in the x-phase upper and lower arms, respectively.

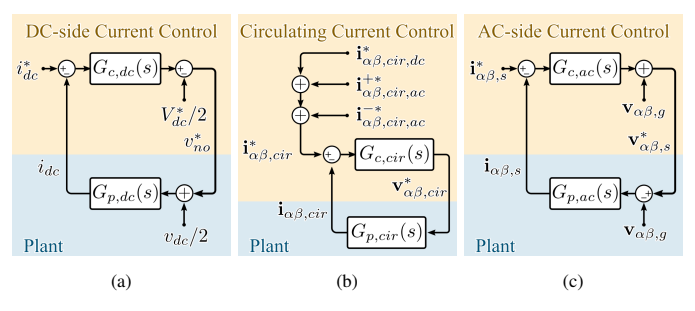


Fig. 4. Block diagrams of decoupled current controls for indirect-modulated MMC and plant transfer functions for each current component. (a) dc-side current, (b) circulating current, (c) ac-side current control loops.

dc current coming from the dc bus. v_{xu} and v_{xl} mean x-phase arm voltage of upper arm and lower arm. The arm voltage is the summed output voltage of SMs in an arm. L_o stands for the inductance of arm inductor, R_o for the resistance of arm inductor, L_s for the inductance of ac-side filter inductor, and R_s for the resistance of ac-side filter.

From arm voltages, the ac-side output voltage, $\mathbf{v}_s = [v_{as} \ v_{bs} \ v_{cs}]^{\top}$ and leg internal voltage, $\mathbf{v}_o = [v_{ao} \ v_{bo} \ v_{co}]^{\top}$ are defined as follows:

$$\mathbf{v}_s = -\frac{1}{2}(\mathbf{v}_u - \mathbf{v}_l), \quad \mathbf{v}_o = -\frac{1}{2}(\mathbf{v}_u + \mathbf{v}_l)$$
(1)

where $\mathbf{v}_u = [v_{au} \ v_{bu} \ v_{cu}]^{\top}$ and $\mathbf{v}_l = [v_{al} \ v_{bl} \ v_{cl}]^{\top}$. From arm currents, the ac-side current, $\mathbf{i}_s = [i_{as} \ i_{bs} \ i_{cs}]^{\top}$,

From arm currents, the ac-side current, $\mathbf{i}_s = [i_{as} \ i_{bs} \ i_{cs}]^{\top}$, and the average of the upper and lower arm currents, $\mathbf{i}_o = [i_{ao} \ i_{bo} \ i_{co}]^{\top}$, are defined as follows:

$$\mathbf{i}_s = \mathbf{i}_u - \mathbf{i}_l, \quad \mathbf{i}_o = \frac{1}{2}(\mathbf{i}_u + \mathbf{i}_l)$$
 (2)

where $\mathbf{i}_u = [i_{au} \ i_{bu} \ i_{cu}]^{\top}$ and $\mathbf{i}_l = [i_{al} \ i_{bl} \ i_{cl}]^{\top}$. From (2), the circulating current, $\mathbf{i}_{o,cir} = [i_{ao,cir} \ i_{bo,cir} \ i_{co,cir}]^{\top}$,

is defined as follows:

$$\mathbf{i}_{o,cir} = \mathbf{i}_o - \frac{1}{3} \begin{bmatrix} i_{dc} & i_{dc} & i_{dc} \end{bmatrix}^{\top}. \tag{3}$$

By applying Kirchhoff's laws to the MMC circuit, the dynamics of the MMC can be represented by decoupled equivalent models for the dc-side current, circulating current, and ac-side current, as illustrated in Fig. 2 (see also [37], [38], and [32]). In the complex frequency domain, the dynamics of the dc-side current shown in Fig. 2(a) can be formulated as follows:

$$i_{dc}(s) = \underbrace{\frac{1}{s\left(\frac{1}{3}L_o\right) + \left(\frac{1}{3}R_o\right)}}_{G_{p,dc}(s)} \left(\frac{v_{dc}(s)}{2} + v_{no}(s)\right), \quad (4)$$

where $v_{no} = (v_{ao} + v_{bo} + v_{co})/3$.

The dynamics of the circulating current shown in Fig. 2(b) and ac-side current shown in Fig. 2(c) can be expressed in the $\alpha\beta$ -frame as follows:

$$\mathbf{i}_{\alpha\beta,cir}(s) = \underbrace{\frac{1}{sL_o + R_o}}_{G_{p,cir}(s)} \mathbf{v}_{\alpha\beta,cir}(s), \tag{5}$$

$$\mathbf{i}_{\alpha\beta,s}(s) = \underbrace{\frac{1}{sL_{ac} + R_{ac}}}_{G_{p,ac}(s)} (\mathbf{v}_{\alpha\beta,s}(s) - \mathbf{v}_{\alpha\beta,g}(s)), \quad (6)$$

where $L_{ac}=L_s+L_o/2$ and $R_{ac}=R_s+R_o/2$. The subscript ' $\alpha\beta$ ' denotes the $\alpha\beta$ -frame components obtained by $\alpha\beta$ transformation, $\mathbf{T}=\begin{bmatrix}2/3 & -1/3 & -1/3 \\ 0 & 1/\sqrt{3} & -1/\sqrt{3}\end{bmatrix}$ as follows:

$$\mathbf{v}_{\alpha\beta,cir} = \mathbf{T}\mathbf{v}_o, \quad \mathbf{i}_{\alpha\beta,cir} = \mathbf{T}\mathbf{i}_{o,cir},$$
 (7)

$$\mathbf{v}_{\alpha\beta,s} = \mathbf{T}\mathbf{v}_s, \quad \mathbf{i}_{\alpha\beta,s} = \mathbf{T}\mathbf{i}_s, \quad \mathbf{v}_{\alpha\beta,g} = \mathbf{T}\mathbf{v}_g,$$
 (8)

where \mathbf{v}_g is the grid voltage defined as $[v_{ag} \ v_{bg} \ v_{cg}]^{\top}$.

Based on the decoupled equivalent models shown in Fig. 2, the decoupled control strategy for the MMC, which is presented in [32], enables independent regulation of the deside current, ac-side current, and capacitor energies in the MMC.

An overview of the decoupled control strategy is illustrated in Fig. 3. Without loss of generality, the inverter-mode operation is considered in this paper as an example. For the outer control loops, capacitor energy controllers - including total energy, leg energy, and upper/lower arm energy controllers—are implemented to balance the capacitor energy of each arm. These energy controllers generate references for i_{dc} and $\mathbf{i}_{\alpha\beta,cir}$ denoted by superscript '*' in Fig. 3. By regulating dc-side current, i_{dc} , the total capacitor energy of all SMs is controlled. The dc component of the circulating current, $\mathbf{i}_{\alpha\beta,cir,dc}$, is controlled to balance the capacitor energy between the legs. The positive and negative ac components of the circulating current, $\mathbf{i}^+_{\alpha\beta,cir,ac}$ and $\mathbf{i}^-_{\alpha\beta,cir,ac}$, are controlled to balance the capacitor energy between the upper and lower arms. The ac-side current, $\mathbf{i}_{\alpha\beta,s}$, is regulated to control the active and reactive power to the ac grid. Since the capacitor energy control is built upon the independent current control of the MMC, the current controllers for i_{dc} , $\mathbf{i}_{\alpha\beta,cir}$, and $\mathbf{i}_{\alpha\beta,s}$ are implemented as inner control loops.

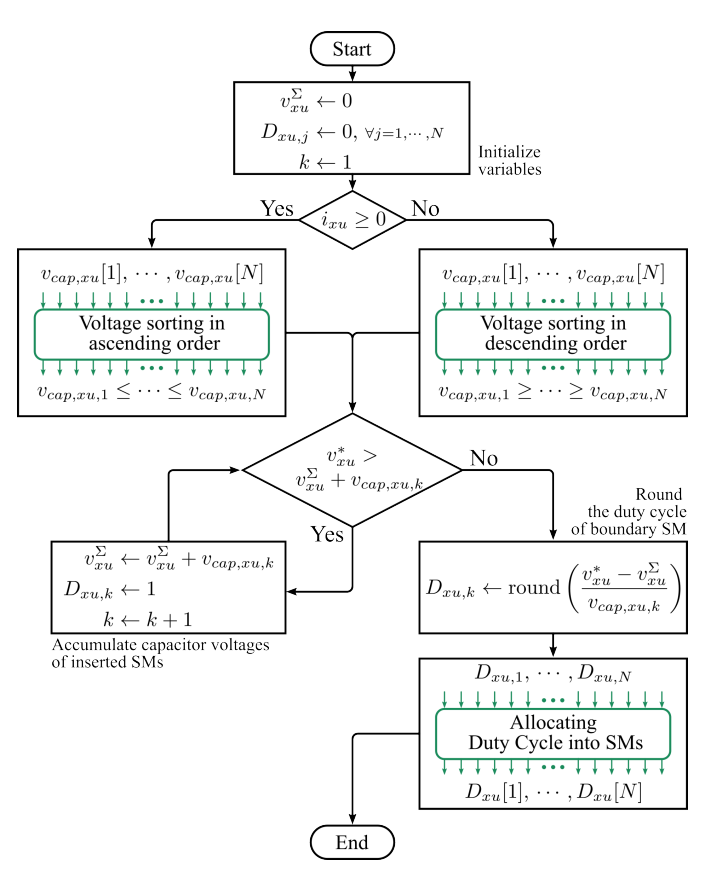


Fig. 5. Operation flowchart of NLM for indirect-modulated MMC to determine duty cycles of SMs in x-phase upper arm. Duty cycles of SMs in lower arm can be determined in the same way. Half-bridge SM is assumed to be used in this flowchart.

Fig. 4 illustrates the block diagrams of the decoupled current controls for the indirect-modulated MMC. To achieve high current control performance, it is assumed that voltage references from the current controllers are accurately applied to the decoupled models of the MMC. It can be realized by precisely synthesizing the arm voltage references, v_{xu}^* and v_{xl}^* , based on the measured capacitor voltages of the SMs, which is known as indirect modulation [31], [32]. Note that the synthesis error in the arm voltage is assumed to be negligible in the case of decoupled control of the indirect-modulated MMC.

B. Nearest Level Modulation in Indirect-Modulated MMC

NLM uses the nearest available voltage level to the desired arm voltage reference [15]. In the case of direct-modulated MMC, the number of inserted SMs is determined based on the nominal capacitor voltage, which does not consider the actual capacitor voltages of the SMs. However, in the case of indirect-modulated MMC, the number of inserted SMs is determined based on the instantaneously measured capacitor voltages of the SMs.

Fig. 5 illustrates the operation flowchart of NLM for indirect-modulated MMC. The duty cycle for each SM in the arm is determined by sequentially summing the measured capacitor voltages of the SMs and comparing this accumulated

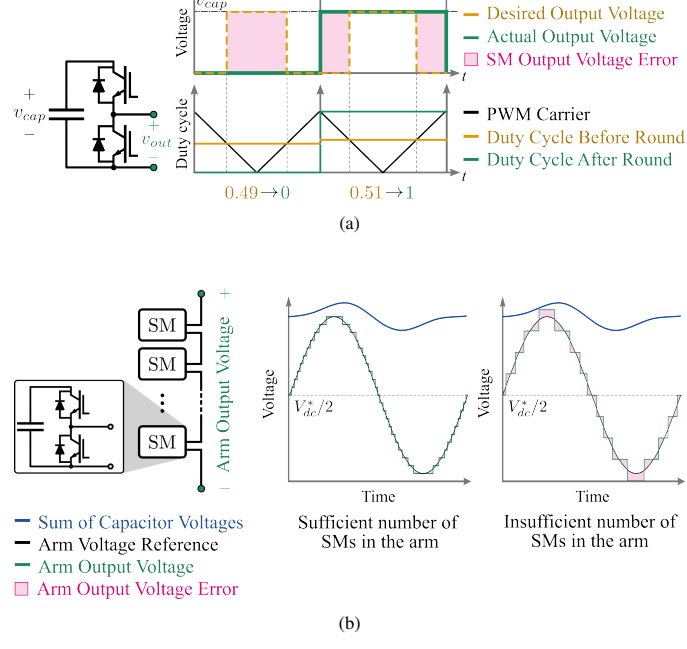


Fig. 6. Conceptual diagram of voltage distortion caused by NLM. (a) Output voltage distortion of boundary SM, (b) Arm voltage distortion caused by NLM depending on the number of SMs in the arm.

value to the arm voltage reference. If the PWM operation is combined with NLM, as described in [10], [11], an SM at the boundary between inserted and bypassed SMs can have a fractional duty cycle between 0 and 1. This boundary SM operates as a PWM switch, to ensure the accurate synthesis of the arm voltage reference. However, in the case of NLM, the insertion of this boundary SM is determined by rounding its duty cycle. If the duty cycle is 0.5 or above, the SM is inserted; otherwise, it is bypassed. Therefore, from the perspective of the arm voltage reference, NLM in indirect-modulated MMC introduces an arm voltage synthesis error of up to half of the capacitor voltage of the boundary SM. Fig. 6(a) shows the conceptual diagram of the output voltage distortion of the corresponding boundary SM.

In HVDC applications, where the number of SMs in each arm is sufficiently large, NLM can be conveniently used for the indirect-modulated MMC since the arm voltage can be synthesized with a sufficient number of levels, therefore, the aforementioned voltage synthesis errors are negligible. For example, in [14], NLM based on the measured capacitor voltages is employed for 400 SMs in the arm of the MMC for HVDC applications, while the decoupled control of the indirect-modulated MMC is employed. However, in the case of small number of SMs per arm, such as those used in MVDC applications, the number of SMs in each arm is limited, and the arm voltage reference cannot be synthesized with a sufficient number of levels. Fig. 6(b) illustrates the conceptual diagram of the arm voltage distortion caused by NLM. Without a sufficient number of SMs or PWM functionality, the arm voltage synthesis error caused by NLM can be significant. Such voltage synthesis error not only degrades the ac-side current quality but also the control performance of circulating

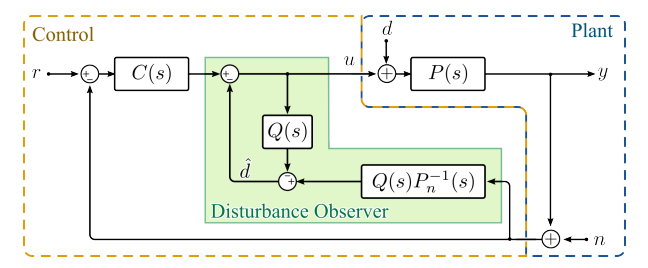


Fig. 7. Block diagram of DOB for a linear plant. C(s), P(s), and Q(s) represent the transfer function for controller, plant, and Q-filter of DOB, respectively. r stands for the reference signal, u for the controller output, y for the output of the plant, n for the noise signal, and d for the disturbance.

current and dc-side current, which are all critical control targets in indirect modulation based control.

C. Principles of Disturbance Observer

Fig. 7 illustrates the structure of a DOB for a linear plant. C(s), P(s), and Q(s) represent the transfer function for the controller, plant, and Q-filter of DOB, respectively. r stands for the reference signal, u for the controller output, y for the output of the plant, n for the noise signal, and d for the disturbance.

In order to consider the parameter uncertainty of the plant, the set of plant transfer functions, \mathcal{P} , to which P(s) belongs, can be defined as follows:

$$\mathcal{P} = \{ g \frac{s^{n-\nu} + \beta_{n-\nu-1} s^{n-\nu-1} + \dots + \beta_0}{s^n + \alpha_{n-1} s^{n-1} + \dots + \alpha_0}$$

$$: \alpha_k \in [\underline{\alpha}_k, \overline{\alpha}_k], \ \beta_k \in [\underline{\beta}_k, \overline{\beta}_k], \ g \in [\underline{g}, \overline{g}] \}, \ \underline{g} > 0, \quad (9)$$

where the interval $[\underline{\alpha}_k, \overline{\alpha}_k]$, $[\underline{\beta}_k, \overline{\beta}_k]$, and $[\underline{g}, \overline{g}]$ represent the uncertainty of the coefficients of the denominator polynomial, the numerator polynomial, and the static gain, respectively. The nominal-parameter plant transfer function is denoted as $P_n(s)$, and it also belongs to \mathcal{P} as P(s) belongs to \mathcal{P} .

The DOB is designed to estimate the disturbance d(s) and compensate it to the output of the controller u(s). The disturbance is assumed to be an unknown input to the plant, P(s). The DOB operates by comparing the estimated plant input, $\hat{u}(s)$, with the controller output, u(s), to estimate the disturbance, $\hat{d}(s)$, and this estimate is then used to compensate for the disturbance in the control loop.

To estimate the plant input, the inverse transfer function of the nominal-parameter plant, $P_n^{-1}(s)$, is used. However, if the plant model, P(s), is a strictly proper transfer function, whose degree of numerator is less than that of denominator, the inverse transfer function of the nominal-parameter plant, $P_n^{-1}(s)$, becomes improper and thus unrealizable. In this case, a Q-filter, Q(s), is used to ensure that $Q(s)P_n^{-1}(s)$ becomes a proper transfer function, thereby making the DOB realizable. Q(s) is implemented as a low-pass filter (LPF) whose denominator degree equals the relative degree of $P_n(s)$, $\nu \in \mathbb{N}_0$, as follows:

$$Q(s) = \frac{a_0}{(\tau s)^{\nu} + a_{\nu-1}(\tau s)^{\nu-1} + \dots + a_1(\tau s) + a_0}, \quad (10)$$

where a_0 and a_k are real-valued coefficients, and $\tau>0$ determines the cut-off frequency of the Q-filter. With these

considerations, the output of the plant, y(s), in Fig. 7 is expressed as follows:

$$y(s) = \frac{P_n(s)P(s)C(s)}{P_n(s)[1 + P(s)C(s)] + Q(s)[P(s) - P_n(s)]}r(s) + \frac{P_n(s)P(s)[1 - Q(s)]}{P_n(s)[1 + P(s)C(s)] + Q(s)[P - P_n(s)]}d(s) - \frac{P(s)[Q(s) + P_n(s)C(s)]}{P_n(s)[1 + P(s)C(s)] + Q(s)[P(s) - P_n(s)]}n(s),$$
(11)

where r(s) and n(s) represent the reference signal and noise signal, respectively.

Following the approach in [36], let ω_Q be the cutoff frequency of Q(s). By approximating $Q(j\omega)\approx 1$ for $|\omega|\ll \omega_Q$ and $Q(j\omega)\approx 0$ for $|\omega|\gg \omega_Q$, output of the plant, y(s), in (11) can be approximated as follows:

$$y(j\omega) \approx \frac{P_n(j\omega)C(j\omega)}{1 + P_n(j\omega)C(j\omega)}r(j\omega) - n(j\omega), \, |\omega| \ll \omega_Q$$
 (12)

under the assumption that all transfer functions in (11) are stable. This input-output relation in (12) indicates that, within the frequency range below the cut-off frequency of the Q-filter, the DOB enables the closed-loop system to follow the nominal input-output behavior while effectively rejecting the disturbance d(s).

D. Stability Conditions for Disturbance Observer

In [35], stability conditions for the control loops employing DOB are derived. To properly design the DOB while ensuring the stability of the control loop, following conditions are assumed:

- 1) C(s) internally stabilizes $P_n(s) \in \mathcal{P}$.
- 2) $\forall P(s) \in \mathcal{P}$ are minimum phase.
- 3) Coefficients of Q(s) in (10) are chosen such that following polynomial, $p_f(s)$, is a Hurwitz polynomial for all $g \in [g, \overline{g}]$.

$$p_f(s) := s^{\nu} + a_{\nu-1}s^{\nu-1} + \dots + a_1s + \frac{g}{g^*}a_0,$$
 (13)

where g^* is the nominal static gain of the plant, $P_n(s)$. Under these conditions, there exists $\tau^* > 0$ such that all transfer functions in (11) are stable for $\tau \in (0, \tau^*]$. It means that the cut-off frequency of Q-filter has a lower bound, since τ must not exceed τ^* in order to guarantee the stability.

The first condition implies that the controller, C(s), should be designed to stabilize $P_n(s)$. Additionally, the numerator and denominator degrees of $P_n(s)$ should match those of the actual plant P(s), even in the presence of parameter uncertainties, because both of P(s) and $P_n(s)$ belong to \mathcal{P} . The second condition implies that both zeros and poles of P(s), which is a rational transfer function for the linear system, should be located in the left half-plane (LHP) of the complex plane. Once the first and second assumptions are satisfied, the DOB for the stable control loop can be implemented by determining coefficients of Q(s) to satisfy the third assumption. The third assumption means that all roots of $p_f(s) = 0$ are located in the LHP or on the imaginary axis. Then, the τ is chosen to be within the range $(0, \tau^*]$.

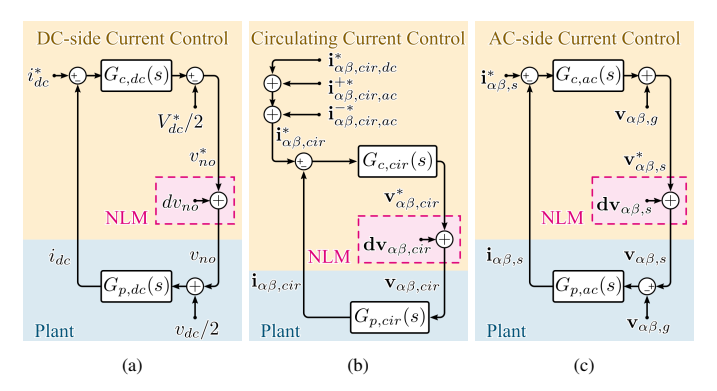


Fig. 8. Equivalent disturbances induced by NLM in decoupled current controls for indirect-modulated MMC. (a) dc-side current, (b) circulating current, (c) ac-side current control loops.

Based on the principles and stability conditions of the DOB discussed in this section, a DOB design to improve the decoupled control of the indirect-modulated MMC under NLM is presented in the following sections.

III. PROPOSED DISTURBANCE OBSERVER DESIGN FOR DECOUPLED CONTROL OF MMC UNDER NLM

In this section, the arm voltage distortion caused by NLM is modeled and decomposed into disturbances affecting the acside current, dc-side current, and circulating current. Based on this disturbance model, the proposed DOB design is presented. For practical applications, a simple implementation is also presented. To ensure the stability of the control loops with the designed DOBs, the proposed method is analyzed based on the stability criterion discussed in Section II-C.

A. Modeling of Disturbances Induced by NLM

For the indirect-modulated MMC, NLM determines the number of inserted SMs in an arm based on the capacitor voltages of each SM and the arm voltage reference. As shown in Fig. 5 and Fig. 6, the duty cycle of the boundary SM between the inserted and bypassed SMs is rounded to either 0 or 1. Therefore, from the perspective of arm-voltage synthesis, NLM in the indirect-modulated MMC introduces the arm voltage error of up to half the capacitor voltage of the boundary SM. As a result, the actual arm voltage is synthesized as follows:

$$v_{xu} = \sum_{k=1}^{N} D_{xu}[k] v_{cap,xu}[k], \quad v_{xl} = \sum_{k=1}^{N} D_{xl}[k] v_{cap,xl}[k],$$

where $D_{xu}[k]$, $D_{xl}[k] \in \{0,1\}$ are the duty cycles. $v_{cap,xu}[k]$ and $v_{cap,xl}[k]$ are the capacitor voltages of the k-th SM in the x-phase upper arm and lower arm, respectively.

The arm voltage error caused by NLM can be interpreted as voltage disturbances formulated as follows:

$$\mathbf{d}\mathbf{v}_u = \mathbf{v}_u - \mathbf{v}_u^*, \quad \mathbf{d}\mathbf{v}_l = \mathbf{v}_l - \mathbf{v}_l^*, \tag{15}$$

where \mathbf{v}_u^* and \mathbf{v}_l^* are the arm voltage references from the current controllers in Fig. 3, while \mathbf{v}_u and \mathbf{v}_l are the actual arm voltages of the upper and lower arms, respectively. $d\mathbf{v}_u =$

 $[dv_{au} \ dv_{bu} \ dv_{cu}]^{\top}$ and $\mathbf{dv}_l = [dv_{al} \ dv_{bl} \ dv_{cl}]^{\top}$ are the arm voltage disturbances caused by NLM at the upper and lower arms, respectively.

Following definitions of the ac-side output voltage and the leg internal voltage in (1), \mathbf{dv}_u and \mathbf{dv}_l also can be equivalently mapped into the ac-side output voltage disturbance, $\mathbf{dv}_s = [dv_{as} \quad dv_{bs} \quad dv_{cs}]^{\mathsf{T}}$, and the leg internal voltage disturbance, $\mathbf{dv}_o = [dv_{ao} \quad dv_{bo} \quad dv_{co}]^{\mathsf{T}}$, as follows:

$$\mathbf{d}\mathbf{v}_{s} = -\frac{1}{2}(\mathbf{d}\mathbf{v}_{u} - \mathbf{d}\mathbf{v}_{l}), \quad \mathbf{d}\mathbf{v}_{o} = -\frac{1}{2}(\mathbf{d}\mathbf{v}_{u} + \mathbf{d}\mathbf{v}_{l}). \quad (16)$$

From the perspective of the decoupled MMC model, the arm voltage error can be equivalently interpreted as a distortion in the output voltage of each decoupled circuit, leading to disturbances in the dc-side current, circulating current, and acside current, individually. The output voltages of each circuit can be formulated with the voltage references and disturbances as follows:

$$v_{no} = v_{no}^* + dv_{no}, (17)$$

$$\mathbf{v}_{\alpha\beta,cir} = \mathbf{v}_{\alpha\beta,cir}^* + \mathbf{d}\mathbf{v}_{\alpha\beta,cir},\tag{18}$$

$$\mathbf{v}_{\alpha\beta,s} = \mathbf{v}_{\alpha\beta,s}^* + \mathbf{d}\mathbf{v}_{\alpha\beta,s},\tag{19}$$

where $\mathbf{dv}_{\alpha\beta,cir} = \mathbf{Tdv}_o$, $\mathbf{dv}_{\alpha\beta,s} = \mathbf{Tdv}_s$, and $dv_{no} = (dv_{ao} + dv_{bo} + dv_{co})/3$.

By substituting (17), (18), (19) into (4), (5), (6), respectively, the decoupled current control loops depicted in Fig. 4 can be redrawn with the corresponding voltage disturbances caused by NLM as shown in Fig. 8. It highlights that the effects of NLM can be equivalently mapped to the voltage disturbances in decoupled models, although NLM operation is conducted for the arm voltage synthesis.

In the following section, the proposed DOB design is presented to increase the rejection capability for the disturbances caused by NLM, consequently improving the decoupled control performance of the MMC under NLM.

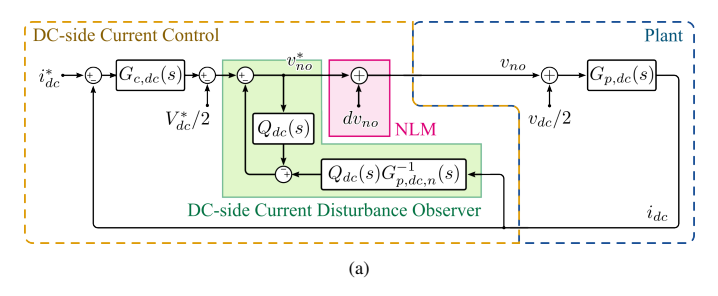
B. Design of Disturbance Observer for NLM

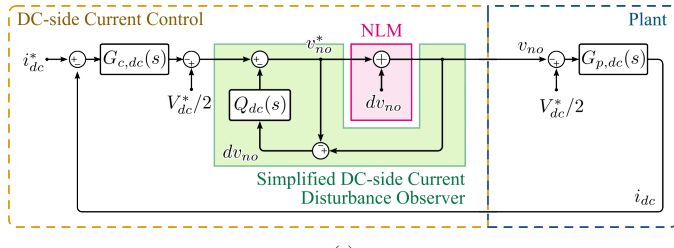
Fig. 9 illustrates the proposed DOB design to improve the decoupled control performance of the MMC under NLM. The DOB is designed for each decoupled equivalent model of the MMC to estimate and compensate the disturbances caused by NLM. For each decoupled model, *Q*-filters are designed as follows:

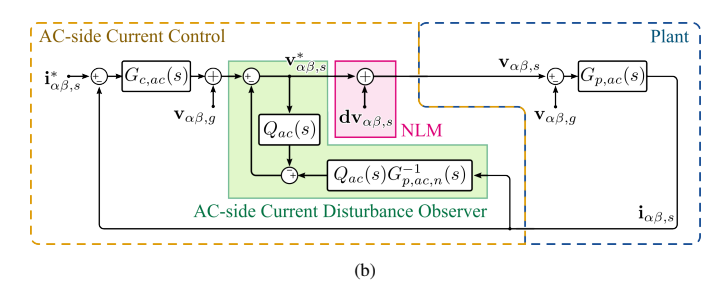
$$Q_x(s) = \frac{a_{0,x}}{\tau_x s + a_{0,x}},\tag{20}$$

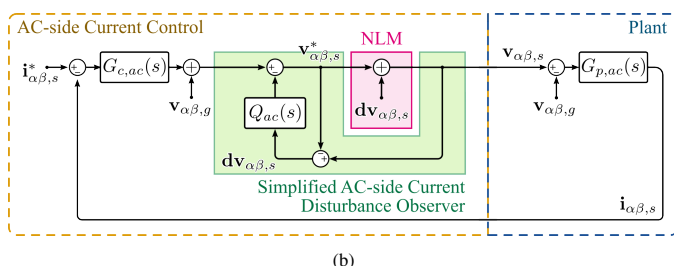
where $x \in \{dc, ac, cir\}$. The subscript 'x' denotes the decoupled model for the dc-side, ac-side, and circulating currents, respectively. $a_{0,x}$ and τ_x stand for the coefficient and time constant of each Q-filter, respectively.

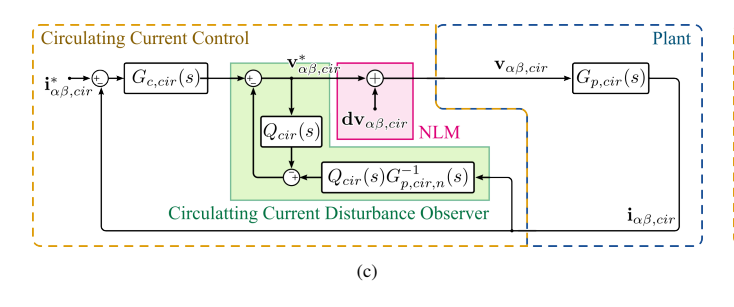
Since the plant for each decoupled model is resistive-inductive (RL) load, whose relative degree is 1, the first order LPF is used as the Q-filter in the DOB based on (10). As shown in Fig. 9, the estimated input of the RL load is obtained by the transfer function combining the Q-filter and the inverse transfer function of the plant. The voltage error is estimated by subtracting the Q-filtered voltage reference from the estimated











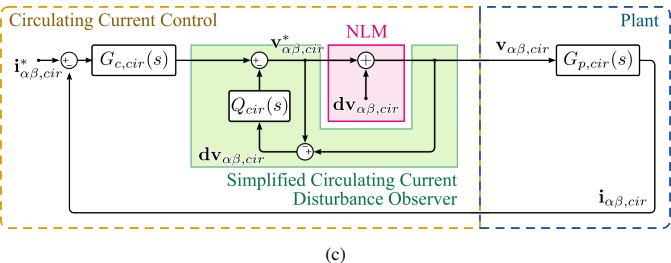


Fig. 9. Proposed DOB design for (a) dc-side current, (b) ac-side current, (c) circulating current control loops. $G_{p,x,n}^{-1}(s), \forall x \in \{dc, ac, cir\}$ denotes the inverse transfer function of the nominal resistive-inductive load for each decoupled model.

Fig. 10. Simplified implementation of the proposed DOB for (a) dc-side current, (b) ac-side current, (c) circulating current control loops.

input to the RL load. This estimated voltage error is then used to compensate in each decoupled control loop.

In principle, the proposed DOB can be implemented as described above. However, for practical purposes, the DOBs in Fig. 9 can be simplified as shown in Fig. 10. Since the arm voltage error is caused by rounding duty cycles of SMs in NLM, it can be directly obtained from the capacitor voltages and duty cycles of the SMs. Based on (15) and (16), dv_s and dv_o can be directly calculated. Consequently, as shown in Fig. 11, the voltage disturbances, $d\mathbf{v}_{\alpha\beta,s}$, $d\mathbf{v}_{\alpha\beta,cir}$, and dv_{no} , which are used as inputs to the Q-filters, can be directly extracted without the need for the inverse transfer function of the RL load in each decoupled model. Therefore, the proposed DOB can be efficiently implemented by directly extracting the voltage disturbances for each decoupled model and applying a single LPF to each current-control loop.

By adopting the proposed DOBs depicted in Fig. 10, the responses of the dc-side, ac-side, and circulating currents to both the current references and the disturbances caused by NLM can be formulated as follows:

$$i_{dc}(s) = T_{r,dc}(s)i_{dc}^*(s) + T_{d,dc}(s)dv_{no}(s),$$
 (21)

$$\mathbf{i}_{\alpha\beta,ac}(s) = T_{r,ac}(s)i_{cir}^*(s) + T_{d,ac}(s)\mathbf{d}\mathbf{v}_{\alpha\beta,ac}(s), \qquad (22)$$

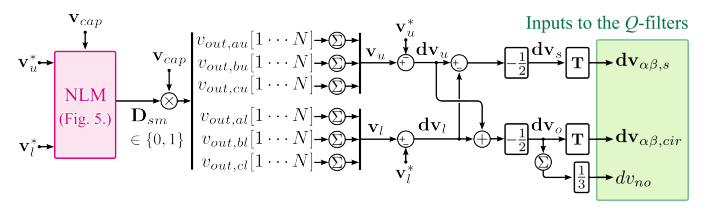


Fig. 11. Implementation of disturbance extraction for the proposed DOB. Extracted voltage disturbances for each decoupled model, $d\mathbf{v}_{\alpha\beta,s}$, $d\mathbf{v}_{\alpha\beta,cir}$, and dv_{no} , are used as the inputs to the Q-filters.

$$\mathbf{i}_{\alpha\beta,cir}(s) = T_{r,cir}(s)\mathbf{i}_{\alpha\beta,cir}^*(s) + T_{d,cir}(s)\mathbf{d}\mathbf{v}_{\alpha\beta,cir}(s),$$
 (23)

where $T_{r,dc}(s)$, $T_{r,ac}(s)$, and $T_{r,cir}(s)$ denote the closed-loop transfer functions from the reference to the current output, while $T_{d,dc}(s)$, $T_{d,ac}(s)$, and $T_{d,cir}(s)$ represent the closedloop transfer functions from the disturbance input to the current output, for each decoupled model. The closed-loop transfer functions from the disturbance and the reference input to the current output are formulated as follows:

$$T_{d,x}(s) = \frac{G_{p,x}(s) (1 - Q_x(s))}{1 + G_{p,x}(s) G_{c,x}(s)},$$
(24)

$$T_{r,x}(s) = \frac{G_{p,x}(s)G_{c,x}(s)}{1 + G_{p,x}(s)G_{c,x}(s)},$$
(25)

where $x \in \{dc, ac, cir\}$.

As shown in (24), the closed-loop system with respect to the disturbance input shows the disturbance rejection capability depending on the Q-filter. By approximating $Q_x(j\omega)\approx 1$ for $|\omega|\ll \omega_{Q,x}$, and $Q_x(j\omega)\approx 0$ for $|\omega|\gg \omega_{Q,x}$, the current responses induced by the disturbance input can be approximated as follows:

$$T_{d,x}(j\omega) \approx 0, \ |\omega| \ll \omega_{Q,x}.$$
 (26)

On the other hand, the closed-loop system with respect to the reference input in (25) exhibits the response characteristics of the designed current controller, independently of NLM. Therefore, the current controller can be designed regardless of NLM operation, while the disturbance effects caused by NLM can be suppressed by the proposed DOB.

By increasing the cut-off frequency of the Q-filter in each decoupled current-control loop, the current quality of each decoupled model can be improved when NLM is applied to the indirect-modulated MMC. Consequently, the cut-off frequency of each Q-filter can be independently adjusted to improve the control quality of the dc-side, ac-side, and circulating currents without interference among them.

C. Stability Analysis of the Proposed Method

Although a larger cut-off frequency of Q-filter leads to the better current-control performance due to the augmented disturbance rejection, the stability of the control loop with the DOB should be considered to ensure the stable operation. For simplicity of analysis, it is assumed that the sampling frequency of the MMC controller is sufficiently high to neglect discretization effects. In addition, all current controllers to regulate the dc-side, ac-side and circulating currents are assumed to be properly designed to stabilize the nominal RL load in corresponding decoupled model. Therefore, the stability of the control loop employing the proposed DOB is analyzed with respect to the second and third conditions discussed in Section II-D, for both the principle-based implementation shown in Fig. 9 and the simplified implementation shown in Fig. 10.

1) Principle-based Implementation: The principle-based implementation of the proposed DOB is shown in Fig. 9. To satisfy the second condition, the transfer function of RL load needs to be the minimum phase. Since R_o , L_o , R_s , and L_s are positive real value, the plant transfer function for each decoupled model has a pole in LHP and no zero, as shown in (4), (5), and (6). Therefore, the plant transfer functions for each current controller are the minimum phase.

To satisfy the third condition, the coefficient and time constant for $Q_{dc}(s)$, $Q_{cir}(s)$, and $Q_{ac}(s)$ should be chosen such that following polynomials are Hurwitz polynomials, meaning that all roots of polynomials are located in LHP.

$$p_{f,dc}(s) = s + \frac{L_o}{L_o^*} a_{0,dc},$$
 (27)

$$p_{f,cir}(s) = s + \frac{L_o}{L_o^*} a_{0,cir},$$
 (28)

$$p_{f,ac}(s) = s + \frac{L_o + \frac{1}{2}L_s}{L_o^* + \frac{1}{2}L_s^*} a_{0,ac},$$
 (29)

where the superscript '*' denotes the nominal parameter value. Under the assumption that L_o , L_o^* , L_s , and L_s^* are positive values, the roots of $p_{f,dc}$, $p_{f,cir}$, and $p_{f,ac}$ are located in LHP for all $a_{0,dc}$, $a_{0,cir}$, $a_{0,ac} > 0$. This is consistent with practical systems, as the inductance of a physical inductor, being a passive component, is always positive. Note that arbitrary positive values for $a_{0,dc}$, $a_{0,cir}$, and $a_{0,ac}$ make $p_{f,dc}$, $p_{f,cir}$, and $p_{f,ac}$ Hurwitz polynomials, which is guaranteed by the physical property that the inductance of a physical inductor is always positive.

By satisfying the first, second and third conditions in Section II-D, there exist positive constants τ_{dc}^* , τ_{cir}^* , and τ_{ac}^* such that the control loops employing the DOB are stable for $\tau_{dc} \in (0, \tau_{dc}^*]$, $\tau_{cir} \in (0, \tau_{cir}^*]$, and $\tau_{ac} \in (0, \tau_{ac}^*]$, respectively.

To properly design τ_x of $Q_x(s)$ in (20), it appears necessary to know the upper bounds of the time constant, τ_x^* , in order to ensure $\tau_x \in (0, \tau_x^*]$. However, instead of directly determining τ_x and $a_{0,x}$ in Q-filter, Q-filter for stable control loop of each decoupled model can be indirectly realized by parameterizing $a_{0,x}$ in $Q_x(s)$ as follows:

$$a_{0,x} = \omega_{Q,x} \tau_x^*, x \in \{dc, cir, ac\}.$$
 (30)

Since $p_{f,dc}(s)$, $p_{f,cir}(s)$, and $p_{f,ac}(s)$ are Hurwitz polynomials for arbitrary positive $a_{0,dc}$, $a_{0,cir}$, and $a_{0,ac}$, there exists positive τ_x^* satisfying (30) for $\omega_{Q,x}>0$. In summary, by substituting (30) into (20), the Q-filters for the decoupled models can be flexibly designed with arbitrary cut-off frequency, $\omega_{Q,x}$, as shown below, while maintaining the stability of the control loops.

$$Q_x(s) = \frac{\omega_{Q,x}}{s + \omega_{Q,x}}, \quad x \in \{dc, cir, ac\}.$$
 (31)

2) Simplified Implementation: The simplified implementation of the proposed DOB is shown in Fig. 10. This realization is the equivalent to the principle-based implementation depicted in Fig. 9, under the assumption that the nominal parameters — L_o^* , L_s^* , R_o^* , and R_s^* — are identical to the actual parameters of the plant, namely L_o , L_s , R_o , and R_s . Therefore, the simplified implementation is a special case of the principle-based implementation. Accordingly, the stability analysis in Section III-C1 remains valid.

For the intuitive understanding, the stability analysis can be simplified based on the transfer functions in (24) and (25). Since the current controllers are assumed to be designed to stabilize the nominal RL load in each model, all poles of $T_{r,x}(s)$ in (25) are located in LHP. It means that solutions of following equation are located in LHP.

$$D_{p,x}(s)D_{c,x}(s) + N_{p,x}(s)N_{c,x}(s) = 0,$$

 $x \in \{dc, cir, ac\},$ (32)

where $D_{p,x}(s)$ and $D_{c,x}(s)$ denote the denominator polynomials of $G_{p,x}(s)$ and $G_{c,x}(s)$, while $N_{p,x}(s)$ and $N_{c,x}(s)$ denote the numerator polynomials of $G_{p,x}(s)$ and $G_{c,x}(s)$, respectively.

By substituting $D_{p,x}(s)$ and $N_{p,x}(s)$, as well as $D_{c,x}(s)$ and $N_{c,x}(s)$, into $G_{p,x}(s)$ and $G_{c,x}(s)$ in (24), respectively, and

TABLE I
PARAMETERS FOR DECOUPLED CURRENT CONTROL

DC-side Current Control				
Controller, $G_{c,dc}(s)$	$K_{p,dc} + K_{i,dc}/s$			
Bandwidth, $\omega_{bw,dc}$	$2\pi \times 100$ rad/s			
Proportional Gain, $K_{p,dc}$ Integral Gain, $K_{i,dc}$	$(L_o/3) \times \omega_{bw,dc}$ $(R_o/3) \times \omega_{bw,dc}$			
AC-side Current Control *				
Controller, $G_{c,ac}(s)$	$K_{p,ac} + K_{i,ac}/s + +K_{r,ac}s/(s^2 + \omega_r^2)$			
Reference frame	Stationary Reference Frame ($\alpha\beta$ -frame)			
Bandwidth, $\omega_{bw,ac}$	$2\pi \times 100$ rad/s			

Controller, $G_{c,ac}(s)$	$K_{p,ac} + K_{i,ac}/s + + K_{r,ac}s/(s^2 + \omega_r^2)$
Reference frame	Stationary Reference Frame ($\alpha\beta$ -frame)
Bandwidth, $\omega_{bw,ac}$	$2\pi \times 100$ rad/s
Proportional Gain, $K_{p,dc}$	$(L_o/2) \times \omega_{bw,ac}$
Integral Gain, $K_{i,dc}$	$(R_o/2) \times \omega_{bw,ac}$
Resonant Gain, $K_{r,cir}$	$(R_o/2) imes \omega_{bw,ac}$

Controller, $G_{c,cir}(s)$	$K_{p,cir} + K_{i,cir}/s + K_{r,cir}s/(s^2 + \omega_r^2)$		
Reference frame	Stationary Reference Frame ($\alpha\beta$ -frame)		
Bandwidth, $\omega_{bw,cir}$	$2\pi \times 100$ rad/s		
Proportional Gain, $K_{p,cir}$	$L_o imes \omega_{bw,cir}$		
Integral Gain, $K_{i,cir}$	$(R_o) imes \omega_{bw,cir}$		
Resonant Gain, $K_{r,cir}$	$(R_o) imes \omega_{bw,cir}$		

^{*} Resonant frequency, ω_r , is set to the ac-side grid frequency obtained by phase-locked loop (PLL)

TABLE II SYSTEM PARAMETERS FOR SIMULATION

Modular Multilevel Converter						
Rated power	1 MW	Number of SM per arm	10			
Rated dc voltage, V_{dc}^*	10 kV	SM nominal dc voltage	1 kV			
Arm inductance, L_o	16 mH	SM capacitance	1 mF			
Arm resistance, R_o	$8~\text{m}\Omega$	Sampling frequency	10 kHz			
AC Grid						
Grid line-to-line voltage*	6.6 kV	Nominal grid frequency	60 Hz			

^{*} Voltage is expressed as its root-mean-square (RMS) value.

further substituting $Q_x(s)$ in (31), $T_{d,x}(s)$ can be rewritten as follows:

$$T_{d,x}(s) = \frac{N_{p,x}(s)D_{c,x}(s)}{D_{p,x}(s)D_{c,x}(s) + N_{p,x}(s)N_{c,x}(s)} \frac{s}{s + \omega_{Q,x}}.$$
(33)

Since $\omega_{Q,x}$ is positive and the solutions of (32) are located in the LHP, all poles of $T_{d,x(s)}$ are also located in the LHP. Therefore, the closed-loop systems described in (21), (22), and (23) are stable for arbitrary cut-off frequency of the Q-filter in each decoupled model.

From a control perspective, increasing the cut-off frequency of the Q-filter in each decoupled current-control loop is desirable for enhancing the decoupled control performance of the MMC under NLM operation, as it does not compromise the stability of the control loops. However, in practice, there exists a trade-off between the cut-off frequency of the Q-filter and the average switching frequency of the SMs. In the following simulation and experimental results, this trade-off is examined, and the effectiveness of the proposed DOB design is validated.

IV. SIMULATION RESULTS

To verify the validity of the proposed DOB design, a simulation of MMC-based DC/AC power conversion is conducted by using PLECS[®]. The control and system parameters are summarized in Table I and Table II, respectively.

In this section, the following aspects are described: 1) It is demonstrated that, for each decoupled current control loop, the voltage disturbance caused by NLM is independently rejected by the proposed DOB. 2) It is demonstrated that, the capacitor voltage balancing is achieved by employing the proposed DOB for dc-side and circulating currents. 3) The effects of the *Q*-filter cut-off frequency on the current quality and the average switching frequency of SMs are numerically investigated.

A. Improvement of Decoupled Current Control

Fig. 12 illustrates effects of DOBs for each decoupled current component, i_{dc} , \mathbf{i}_s , and \mathbf{i}_o . The cut-off frequency of the Q-filter for each DOB is set to half of the sampling frequency.

In Fig. 12(a), all proposed DOBs are initially deactivated for $t < 0 \, \text{s}$. At $t = 0 \, \text{s}$, only the DOB for ac-side current is activated. As a result, the ac-side current restores three-phase balance and the harmonic distortion is conspicuously reduced, while the dc-side current is barely affected. It is observed that the circulating current is slightly improved. This is because the ac-side output power is stably regulated by the proposed DOB for ac-side current for $t > 0 \, \text{s}$, which indirectly helps mitigate the irregular energy imbalance between the arms. Consequently, the circulating current, carrying the power between arms, is improved to some extent. However, its improvement is limited since the disturbance caused by NLM operation for circulating current is not directly addressed.

Similarly, Fig. 12(b) demonstrates that the DOB for the deside current effectively suppresses the fluctuation in i_{dc} . Fig. 12(c) shows that the DOB for the circulating current mitigates its irregular fluctuations. The improvement in circulating current is not as notable as that in the dc or ac-side currents; however, as will be discussed later, it brings significant enhancement in capacitor energy control. These results in Fig. 12 validate that the proposed DOB can be independently applied to each decoupled current component, effectively rejecting the corresponding NLM-induced disturbance.

The arm voltages illustrated in Fig. 12(d), (e), and (f), show magnified views of the arm voltages from 0 ms to 10 ms, corresponding to Fig. 12(a), (b), and (c), respectively. The minimum pulse width of the arm voltage is the same with the sampling period, 100 μs , because NLM operation is employed.

Fig. 13 illustrates the effects of the DOB cut-off frequency on the ac-side current quality. Total harmonic distortion (THD) and dc bias of the ac-side current are observed under various cut-off frequencies of the DOB for ac-side current, ranging from 0% to 50% of the sampling frequency, while cut-off frequencies of the other DOBs are fixed to half of the sampling frequency. As the cut-off frequency increases, THD of the ac-side current decreases, as shown in Fig. 13(a). Furthermore, the proposed DOB mitigates the dc bias of the ac-side current, as depicted in Fig. 13(b). This is a significant advantage because such a dc component can cause asymmetric magnetic core saturation in the ac-side transformer [39].

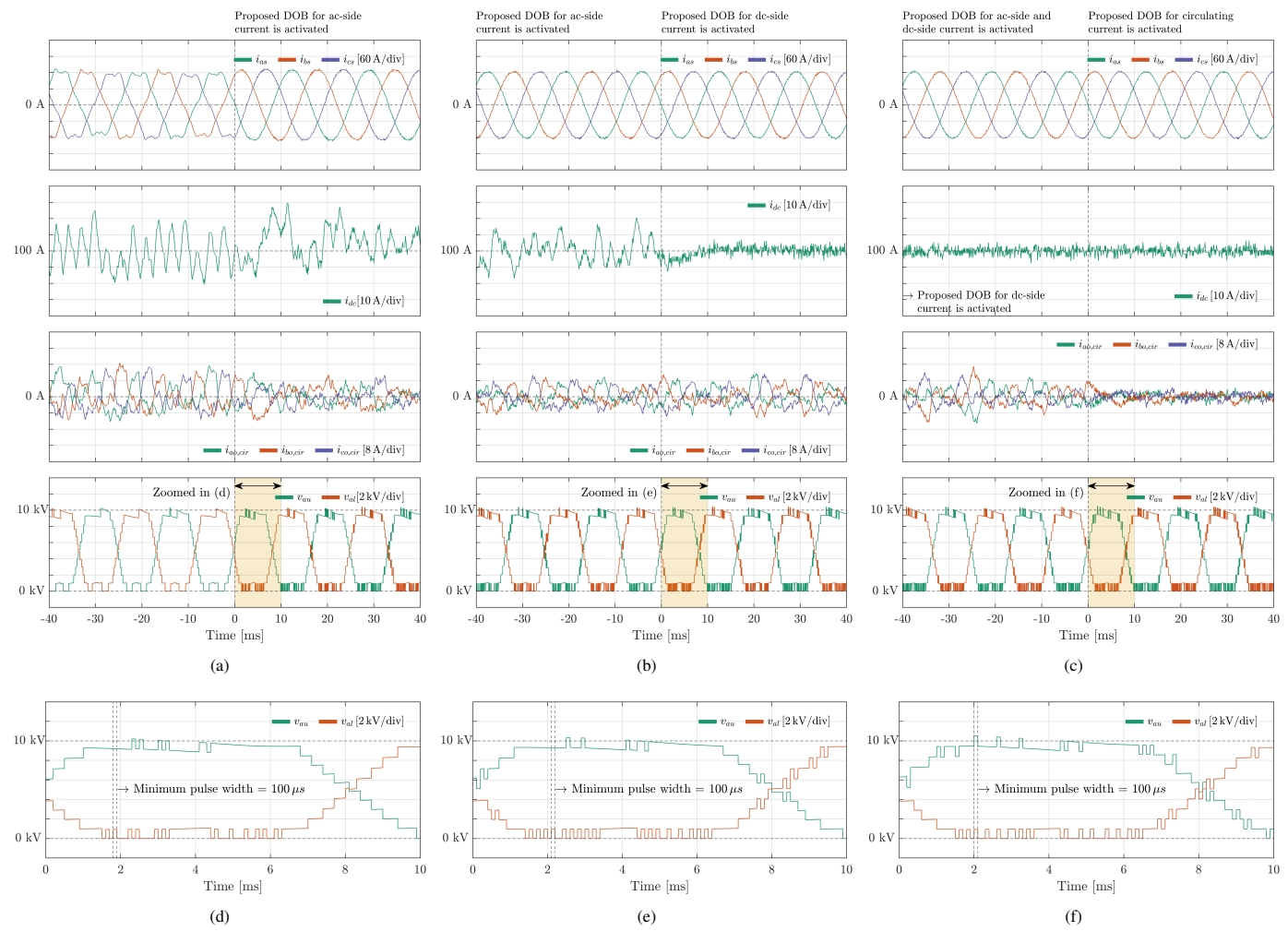


Fig. 12. Simulation results representing the effects of the DOB on (a) ac-side current, (b) dc-side current, and (c) circulating current. For case (a), only the DOB for ac-side current is activated at t = 0 s. For case (b), the DOB for dc-side current is activated at t = 0 s while only the DOB for ac-side current is initially activated. For case (c), the DOB for circulating current is activated at t = 0 s while the DOBs for ac-side and dc-side currents are initially activated. Arm voltages shown in (d), (e), and (f) present magnified views of the arm voltages from 0 ms to 10 ms, corresponding to (a), (b), and (c), respectively.

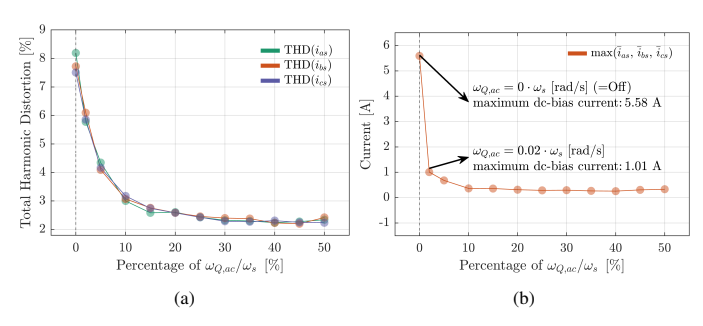


Fig. 13. Simulation results showing the effects of the DOB cut-off frequency for ac-side current on (a) total harmonic distortion (THD) and (b) dc bias of the ac-side current. \bar{i}_x , indicates the average value of $i_{x\in\{as,bs,cs\}}$ over a fundamental period. $\max(\cdot)$ represents the maximum value among three phases. ω_s represents the angular sampling frequency in rad/s.

B. Improvement of Capacitor Voltage Balancing

Fig. 14 illustrates the effects of the proposed DOBs on capacitor voltage balancing. $\mathbf{E}^{\Sigma}_{abc}$ and $\mathbf{E}^{\Delta}_{abc}$ are represented as $\mathbf{E}^{\Sigma}_{\alpha\beta0} = [E^{\Sigma}_{\alpha} \ E^{\Sigma}_{\beta} \ E^{\Sigma}_{0}]^{\top}$ and $\mathbf{E}^{\Delta}_{\alpha\beta0} = [E^{\Delta}_{\alpha} \ E^{\Delta}_{\beta} \ E^{\Delta}_{0}]^{\top}$ in the $\alpha\beta0$ -frame, respectively, by using Clarke transformation. In Fig. 14(a), only the DOB for ac-side current is

activated for t<0 s. At t=0 s, the DOB for dc-side current is activated. As a result, the total capacitor energy in MMC, E_{total} , is properly regulated to its nominal value, by achieving the proper dc-side current reference tracking via the proposed DOB. However, since the circulating current is not well regulated, $\mathbf{E}_{\alpha\beta}^{\Sigma}$ and $\mathbf{E}_{\alpha\beta0}^{\Delta}$ are irregularly fluctuated, as shown in the third and fourth plots of Fig. 14(a).

In Fig. 14(b), the DOB for circulating current is additionally activated. By suppressing the disturbance in the circulating current, $\mathbf{E}_{\alpha\beta}^{\Sigma}$ and $\mathbf{E}_{\alpha\beta0}^{\Delta}$ are effectively controlled to converge to zero. Consequently, the capacitor voltages of all SMs are balanced, as shown in the first plot of Fig. 14(b).

C. Trade-off in DOB Cut-off Frequency

Despite the benefits of the proposed DOB as aforementioned, there exists a trade-off in selecting the cut-off frequency of the *Q*-filter. As shown in Fig. 12(d), (e), and (f), enabling DOB causes the arm voltage to exhibit pseudo-PWM behavior, even under NLM operation. This behavior increases the averaged switching frequency of SMs, which can lead to higher switching losses. This trade-off is numerically

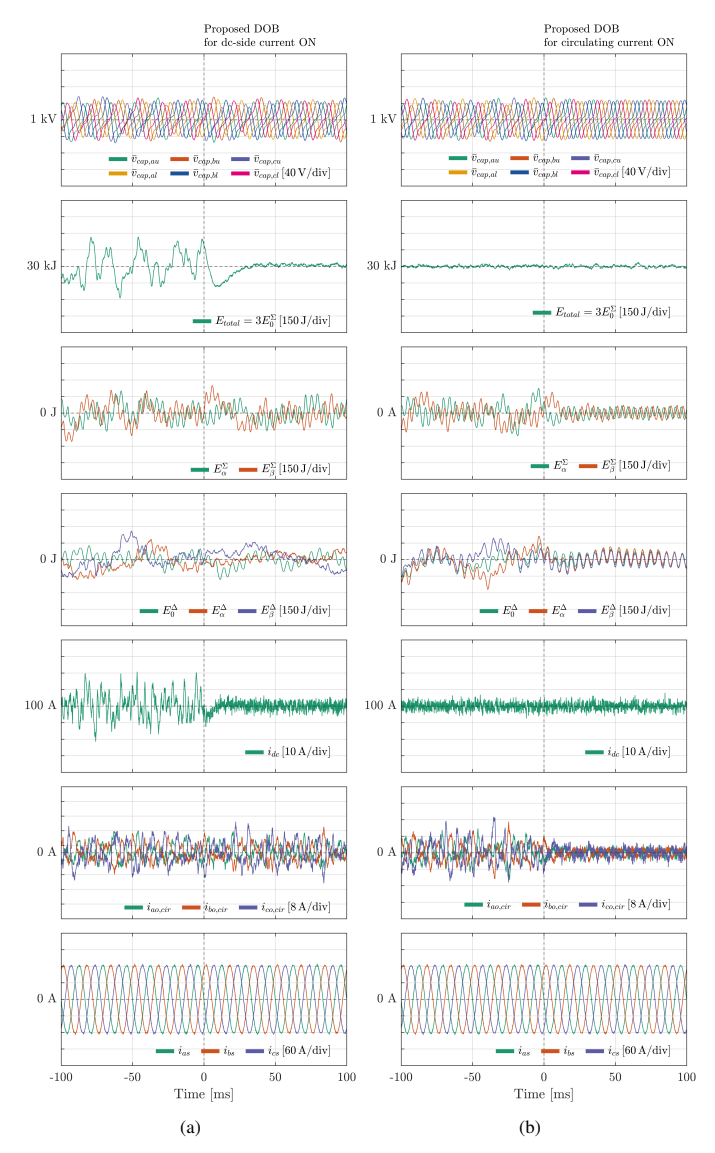


Fig. 14. Simulation results showing the effects of DOBs on capacitor voltage balancing. (a) DOB for dc-side current is activated at $t=0\,\mathrm{s}$ while only the DOB for ac-side current is initially activated. (b) DOB for circulating current is activated at $t=0\,\mathrm{s}$, while the DOBs for the ac-side and dc-side currents are initially activated.

investigated in this section, by varying the cut-off frequency of each DOB. An analytical approach needs to be further studied.

Fig. 15(a) illustrates the effects of the DOB cut-off frequency on the SM-averaged switching frequency. As the cut-off frequency of DOB increases, the switching frequency of SMs also increases. On the other hand, THD of the acside is affected only by the cut-off frequency of the DOB for ac-side current, as shown in Fig. 15(b). Therefore, a practical tuning approach is to set a low cut-off frequency for the circulating current DOB—addressing switching loss concerns—while employing high cut-off frequencies for the ac- and dc-side current DOBs to ensure high-quality current for grid interaction. The waveforms in Fig. 14(b) for t < 0 s exemplify this tuning approach. In this interval, the ac- and dc-side DOBs are active, while the circulating current DOB is disabled, representing the extreme case of setting its cut-

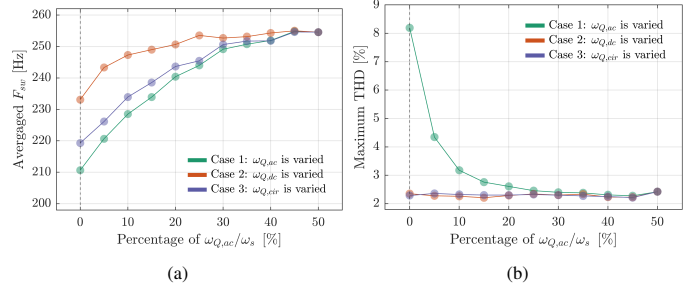


Fig. 15. Simulation results showing the effects of the DOB cut-off frequency on (a) SM-averaged switching frequency and (b) THD variation of the acside current. Case 1, 2, and 3 represent that only the cut-off frequency of the DOB for ac-side, dc-side, and circulating current is varied, respectively, while the cut-off frequencies of the other DOBs are fixed to half of the sampling frequency. ω_s represents the angular sampling frequency in rad/s.

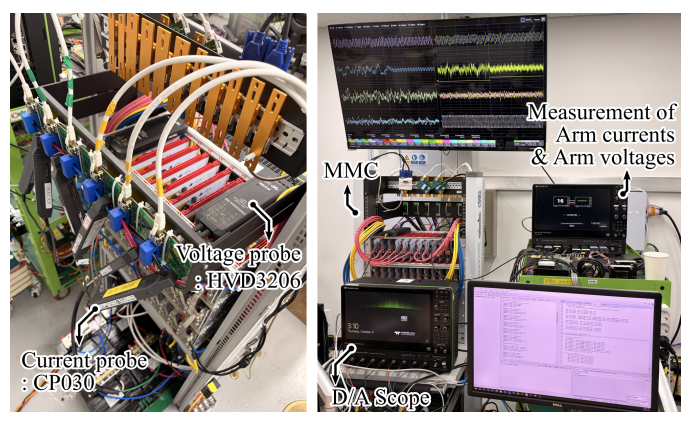


Fig. 16. Experimental setup.

TABLE III
SYSTEM PARAMETERS FOR EXPERIMENT

Modular Multilevel Converter						
Rated power	5 kW	Number of SM per arm	6			
Rated dc voltage, V_{dc}^*	360 V	SM nominal dc voltage	60 V			
Arm inductance, L_o	4 mH	SM capacitance	2.39 mF			
Arm resistance, R_o	$23~\text{m}\Omega$	Sampling frequency	7.2 kHz			
AC Grid						
Grid line-to-line voltage*	200 V	Nominal grid frequency	60 Hz			

Voltage are expressed as its root-mean-square (RMS) value.

off frequency to zero to minimize its impact on switching frequency. This strategy is particularly effective when precise capacitor voltage balancing is not a primary requirement.

V. EXPERIMENTAL RESULTS

To validate the effectiveness and feasibility of the proposed DOB design, a small-scale hardware experimental setup is implemented, which is shown in Fig. 16. The system parameters for experiment are summarized in Table III. Control parameters are the same as those in the simulation, as shown in Table I. The six arm currents are measured using CP030® current probes, while the *a*-phase upper and lower arm voltages are measured with HVD3206® voltage probes. All signals are sampled at 5 MS/s. Control variables, such

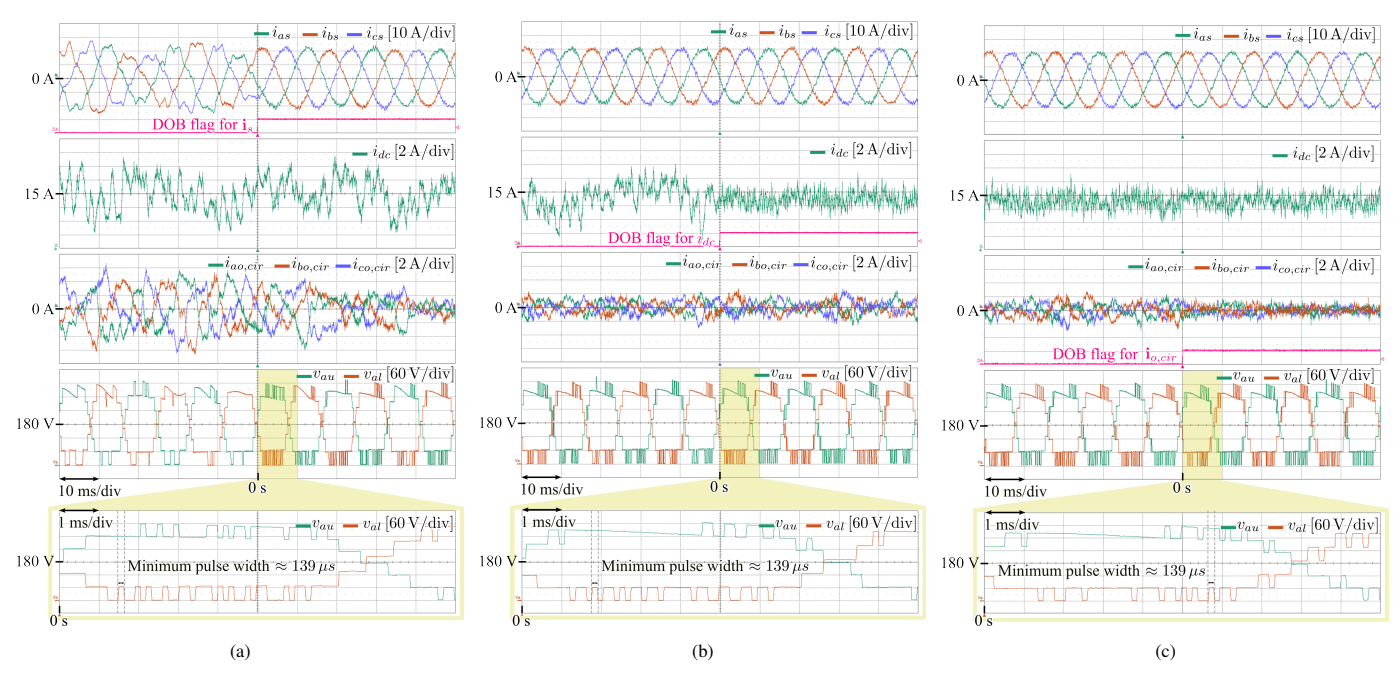


Fig. 17. Experimental results showing the effects of the DOB on (a) ac-side current, (b) dc-side current, and (c) circulating current. For (a) case, only the DOB for ac-side current is activated at t=0 s. For (b) case, the DOB for dc-side current is activated at t=0 s while only the DOB for ac-side current is initially activated. For (c) case, the DOB for circulating current is activated at t=0 s while the DOBs for ac-side and dc-side currents are initially activated.

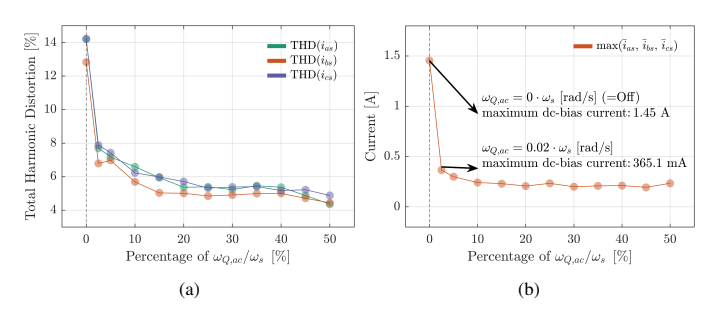


Fig. 18. Experimental results showing the effects of the ac-side DOB's cutoff frequency on (a) total harmonic distortion and (b) dc bias of the ac-side current. The cut-off frequency is normalized to the angular sampling frequency, ω_s . \bar{i}_x indicates the average value of $i_{x\in\{as,bs,cs\}}$ over a fundamental period. $\max(\cdot)$ represents the maximum value among three phases.

as capacitor energy, are captured through 8-channel digital-to-analog converter. Two 8-channel oscilloscopes are used and synchronized via OscilloSYNC $^{\text{TM}}$ to simultaneously capture all signals.

A. Improvement of Decoupled Current Control

Fig. 17 shows the effects of the proposed DOB on the decoupled current control in experiment. The cut-off frequency of the Q-filter for each DOB is set to half of the sampling frequency, $2\pi \times 3600$ rad/sec.

In Fig. 17(a), the DOB for ac-side current is activated while the DOBs for dc-side and circulating currents are deactivated. As a result, the ac-side current restores three-phase balanced sinusoidal waveforms, while the dc-side current is left unaffected. As aforementioned in Section IV-A, it is observed that irregular fluctuation in circulating current $\mathbf{i}_{o,cir}$ is reduced to some extent, because the ac-side output power is

stably regulated by the proposed DOB for ac-side current for t>0 s. However, since the DOB for circulating current is not activated, its improvement is limited compared to the cases when the DOB for circulating current is activated, which is shown in Fig. 17(c).

Fig. 17(b) shows the results when the DOB for dc-side current is activated while the DOB for ac-side current is initially activated. Similarly, the DOB for dc-side current effectively suppresses the current distortion in i_{dc} without affecting the circulating current. Fig. 17(c) shows the results when the DOB for circulating current is activated while the DOBs for ac-side and dc-side currents are initially activated. As a result, the irregular fluctuation in $i_{o,cir}$ is effectively regulated. As seen in the magnified arm voltage waveform, the minimum pulse width is observed as one sampling period due to NLM operation. Notably, these results in Fig. 17 represent that the proposed DOB can be individually applied to each decoupled current control to improve the disturbance rejection capability from NLM operation.

Fig. 18 shows the relationship between the cut-off frequency of DOB for the ac-side current and the quality of the ac-side current, specifically its THD and dc bias. Similar to the simulation results depicted in Fig. 13, the THD and dc bias current decrease as the cut-off frequency increases.

B. Improvement of Capacitor Voltage Balancing

Fig. 19 shows the effects of the proposed DOB on the capacitor voltage balancing in experiment. Differential components of \mathbf{E}^Σ_{abc} are represented as $\mathbf{E}^\Sigma_{\alpha\beta} = [E^\Sigma_\alpha \quad E^\Sigma_\beta]^\top$ in the $\alpha\beta$ frame, while those of \mathbf{E}^Δ_{abc} are represented as $\mathbf{E}^\Delta_{\alpha\beta} = [E^\Delta_\alpha \quad E^\Delta_\beta]^\top$ in the $\alpha\beta$ -frame. Common components of \mathbf{E}^Σ_{abc} and \mathbf{E}^Δ_{abc} are corresponded as E^Σ_0 and E^Δ_0 , respectively.

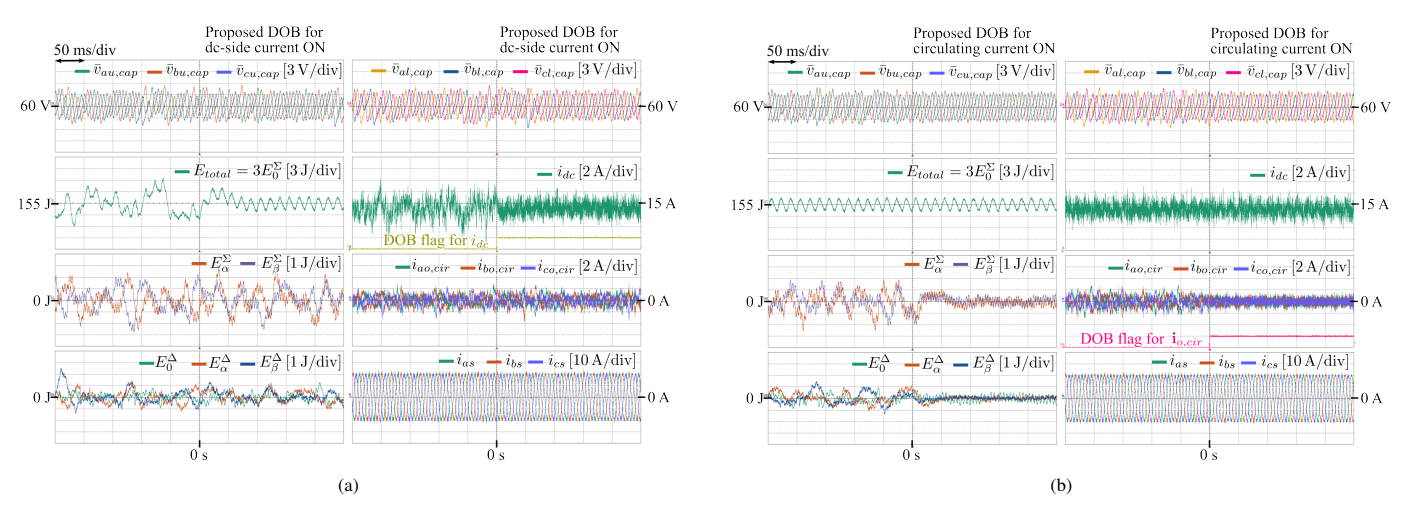


Fig. 19. Experimental results representing the effects of DOB on the capacitor energy (voltage) balancing. (a) DOB for dc-side current is activated at t=0 s while only the DOB for ac-side current is initially activated. (b) DOB for circulating current is activated at t=0 s, while the DOBs for ac-side and dc-side currents are initially activated.

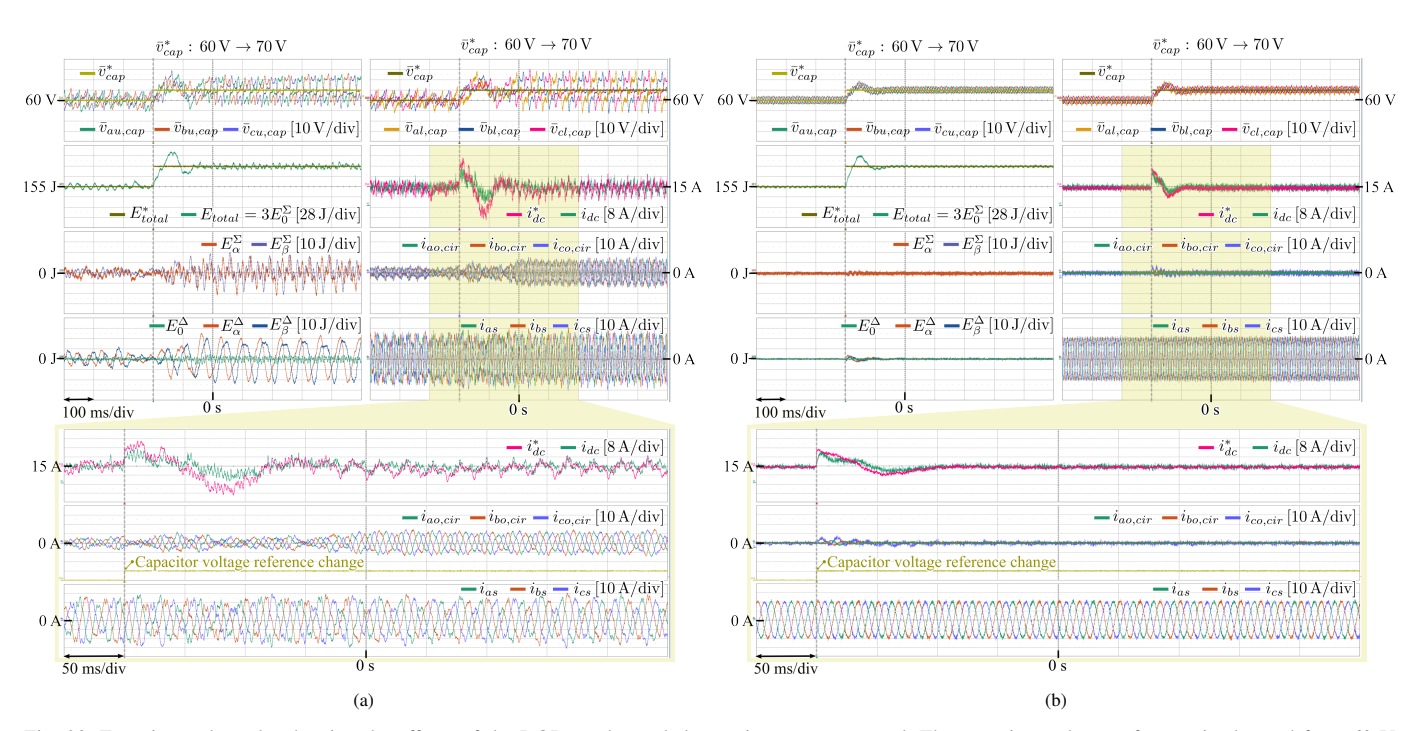


Fig. 20. Experimental results showing the effects of the DOB on decoupled capacitor energy control. The capacitor voltage reference is changed from 60 V to 70 V at t=-0.2 s (a) without DOB and (b) with DOB for each decoupled current control. The superscript '*' indicates the reference value.

In Fig. 19(a), the DOB for dc-side current is activated at t=0 s while only the DOB for ac-side current is initially activated. As a result, the total capacitor energy, E_{total} , is well regulated to its rated value by improving the dc-side current quality via the proposed DOB. However, $\mathbf{E}_{\alpha\beta}^{\Sigma}$ and $\mathbf{E}_{\alpha\beta0}^{\Delta}$ are not improved as shown in the third and fourth plots of Fig. 19(a), because the NLM-induced disturbance for circulating current is still not addressed.

In Fig. 19(b), the DOB for circulating current is activated at $t=0\,\mathrm{s}$, while the DOBs for ac-side and dc-side currents are initially activated. As a result, not only E_{total} but also $\mathbf{E}_{\alpha\beta}^{\Sigma}$ and $\mathbf{E}_{\alpha\beta0}^{\Delta}$ are well regulated to zero. Consistent with the simulation results, the improved circulating current quality directly contributes to effective capacitor energy balancing. As

shown in the first plot of Fig. 19(b), the capacitor voltage balancing is enhanced.

C. Effectiveness in Decoupled Capacitor Energy Control

Fig. 20 shows the effects of the proposed DOB on the decoupled capacitor energy control in experiment. Since the indirect-modulated MMC can offer a control capability for SM capacitor energy decoupled from the ac-side current control as well as the dc-link voltage, the SM capacitor voltage reference is boosted up from 60 V to 70 V at t=-0.2 s by drawing dc-link current instantaneously, while maintaining the ac-side active power and the dc-link voltage at 360 V unchanged.

In Fig. 20(a), the capacitor voltage reference is changed without the proposed DOB. As a result, the capacitor energy

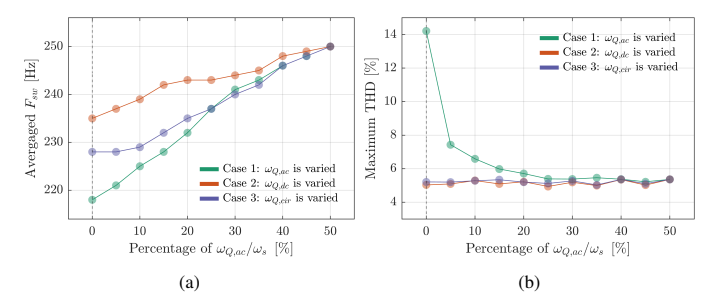


Fig. 21. Experimental results showing the effects of the DOB cut-off frequency on (a) SM-averaged switching frequency and (b) THD variation of the acside current. Case 1, 2, and 3 represent that only the cut-off frequency of the DOB for ac-side, dc-side, and circulating current is varied, respectively, while the cut-off frequencies of the other DOBs are fixed to half of the sampling frequency.

components, $\mathbf{E}^\Sigma_{\alpha\beta}$ and $\mathbf{E}^\Delta_{\alpha\beta0}$, are not regulated to zero, causing large fluctuations in the capacitor voltages. These voltage fluctuations exacerbate the NLM-induced arm voltage synthesis error. Consequently, the ac-side current quality is significantly degraded, and a large circulating current is induced.

In Fig. 20(b), the capacitor voltage reference is changed with the proposed DOB for each decoupled current control all activated. The cut-off bandwidth of Q-filter for each DOB is set to half of the sampling frequency. As a result, the capacitor energy components, $\mathbf{E}_{\alpha\beta}^{\Sigma}$ and $\mathbf{E}_{\alpha\beta0}^{\Delta}$, are clearly regulated to zero. During the transient period following the reference change, a slight deviation is observed in $\mathbf{E}_{\alpha\beta0}^{\Delta}$. However, the system promptly restores the balance by temporarily injecting a corresponding circulating current. Once the capacitor energy reaches a balanced state at the new reference, the circulating current is regulated back to zero, which is the nature of indirect modulation based control. These results demonstrate that the proposed DOB enables decoupled control of capacitor energy for an indirect-modulated MMC with a low number of SMs, even under the constraint of NLM operation.

D. Trade-off in DOB Cut-off Frequency

As discussed in Section IV-C, a trade-off exists between the disturbance rejection performance of the DOB and the resulting switching frequency.

This relationship is experimentally investigated in Fig. 21, which illustrates the SM-averaged switching frequency and the ac-side current THD as the cut-off frequency of each DOB is individually varied. Fig. 21(a) confirms that increasing the cut-off frequency of any DOB leads to a higher average switching frequency. This is because, in principle, a wider DOB bandwidth allows for the compensation of higher-frequency disturbances, which in turn requires more frequent switching actions

Fig. 21(b) shows that the THD of the ac-side current is predominantly influenced by its own DOB (Case 1). Increasing the cut-off frequency for the ac-side DOB significantly improves the current quality by reducing the THD. In contrast, varying the cut-off frequencies of DOBs for the dc-side and circulating currents has a negligible effect on the ac-side current THD. These experimental findings are consistent with the simulation results.

VI. CONCLUSION

In this paper, a new control method based on DOB is proposed to enable fully decoupled control of indirect-modulated MMC under the constraint of NLM operation with a small number of SMs per arm. The proposed method estimates the arm voltage synthesis error inherent in NLM and compensates for it as a disturbance in the ac-side, dc-side, and circulating current control loops. A key advantage of the proposed method is its ease of implementation, as it requires only LPF for the proposed method and no modifications to the conventional NLM and decoupled control structure. Furthermore, since the proposed method is designed to selectively improve the acside, dc-side, and circulating current dynamics, it can offer flexible performance tuning without interference among the respective currents. The validity and effectiveness of the proposed method in improving current quality and decoupled SM energy control are verified through both simulation and experimental results.

REFERENCES

- S. Cui, J.-H. Lee, J. Hu, R. W. De Doncker, and S.-K. Sul, "A modular multilevel converter with a zigzag transformer for bipolar mvdc distribution systems," *IEEE Transactions on Power Electronics*, vol. 34, no. 2, pp. 1038–1043, 2019.
- [2] J. A. Ansari, C. Liu, and S. A. Khan, "Mmc based mtdc grids: A detailed review on issues and challenges for operation, control and protection schemes," *IEEE Access*, vol. 8, pp. 168 154–168 165, 2020.
- [3] S. Cui, J. Hu, and R. De Doncker, "Fault-tolerant operation of a tlc-mmc hybrid dc-dc converter for interconnection of mvdc and hvdc grids," *IEEE Transactions on Power Electronics*, vol. 35, no. 1, pp. 83–93, 2020
- [4] M. A. Perez, S. Ceballos, G. Konstantinou, J. Pou, and R. P. Aguilera, "Modular multilevel converters: Recent achievements and challenges," *IEEE Open Journal of the Industrial Electronics Society*, vol. 2, pp. 224–239, 2021.
- [5] P. Sun, Y. Tian, J. Pou, and G. Konstantinou, "Beyond the mmc: Extended modular multilevel converter topologies and applications," *IEEE Open Journal of Power Electronics*, vol. 3, pp. 317–333, 2022.
- [6] W. Zhang, Q. Gao, B. Su, M. Jin, D. Xu, and J. Liu, "Research on the control strategy of statcom based on modular multilevel converter," in 2014 International Power Electronics Conference (IPEC-Hiroshima 2014 - ECCE ASIA), 2014, pp. 614–618.
- [7] J.-M. Kim, S. Cui, and J.-J. J. Jung, "A new e-statcom topology based on single-star multilevel converter with centralized energy storage and zigzag transformer," *IEEE Transactions on Power Electronics*, pp. 1–17, 2025.
- [8] M. Hagiwara, K. Nishimura, and H. Akagi, "A medium-voltage motor drive with a modular multilevel pwm inverter," *IEEE Transactions on Power Electronics*, vol. 25, no. 7, pp. 1786–1799, 2010.
- [9] J.-J. Jung, H.-J. Lee, and S.-K. Sul, "Control strategy for improved dynamic performance of variable-speed drives with modular multilevel converter," *IEEE Journal of Emerging and Selected Topics in Power Electronics*, vol. 3, no. 2, pp. 371–380, 2015.
- [10] S. Rohner, S. Bernet, M. Hiller, and R. Sommer, "Modulation, losses, and semiconductor requirements of modular multilevel converters," *IEEE Transactions on Industrial Electronics*, vol. 57, no. 8, pp. 2633– 2642, 2010.
- [11] Y. Wang, C. Hu, R. Ding, L. Xu, C. Fu, and E. Yang, "A nearest level pwm method for the mmc in dc distribution grids," *IEEE Transactions* on *Power Electronics*, vol. 33, no. 11, pp. 9209–9218, 2018.
- [12] M. H. Nguyen, S. Kwak, and T. Kim, "Phase-shifted carrier pulse-width modulation algorithm with improved dynamic performance for modular multilevel converters," *IEEE Access*, vol. 7, pp. 170 949–170 960, 2019.
- [13] J. Yin, N. Dai, S. Vazquez, A. Marquez, J. I. Leon, M. A. Perez, and L. G. Franquelo, "An improved indirect pulsewidth modulation technique for modular multilevel converters," *IEEE Transactions on Power Electronics*, vol. 39, no. 1, pp. 733–743, 2024.
- [14] A. E. Leon and S. J. Amodeo, "Energy balancing improvement of modular multilevel converters under unbalanced grid conditions," *IEEE Transactions on Power Electronics*, vol. 32, no. 8, pp. 6628–6637, 2017.

- [15] P. M. Meshram and V. B. Borghate, "A simplified nearest level control (nlc) voltage balancing method for modular multilevel converter (mmc)," *IEEE Transactions on Power Electronics*, vol. 30, no. 1, pp. 450–462, 2015.
- [16] P. Hu and D. Jiang, "A level-increased nearest level modulation method for modular multilevel converters," *IEEE Transactions on Power Electronics*, vol. 30, no. 4, pp. 1836–1842, 2015.
- [17] L. Lin, Y. Lin, Z. He, Y. Chen, J. Hu, and W. Li, "Improved nearest-level modulation for a modular multilevel converter with a lower submodule number," *IEEE Transactions on Power Electronics*, vol. 31, no. 8, pp. 5369–5377, 2016.
- [18] M. H. Nguyen and S. Kwak, "Nearest-level control method with improved output quality for modular multilevel converters," *IEEE Access*, vol. 8, pp. 110 237–110 250, 2020.
- [19] J. Yin, J. I. Leon, M. A. Perez, L. G. Franquelo, A. Marquez, B. Li, and S. Vazquez, "Variable rounding level control method for modular multilevel converters," *IEEE Transactions on Power Electronics*, vol. 36, no. 4, pp. 4791–4801, 2021.
- [20] S. Debnath, J. Qin, B. Bahrani, M. Saeedifard, and P. Barbosa, "Operation, control, and applications of the modular multilevel converter: A review," *IEEE Transactions on Power Electronics*, vol. 30, no. 1, pp. 37–53, 2015.
- [21] A. Antonopoulos, L. Angquist, and H.-P. Nee, "On dynamics and voltage control of the modular multilevel converter," in 2009 13th European Conference on Power Electronics and Applications, 2009, pp. 1–10.
- [22] Q. Tu, Z. Xu, H. Huang, and J. Zhang, "Parameter design principle of the arm inductor in modular multilevel converter based hvdc," in 2010 International Conference on Power System Technology, 2010, pp. 1–6.
- [23] B. Jacobson, P. Karlsson, G. Asplund, L. Harnefors, and T. U. Jonsson, "Vsc-hvdc transmission with cascaded two-level converters," 2010. [Online]. Available: https://api.semanticscholar.org/CorpusID: 114708164
- [24] Q. Tu, Z. Xu, and L. Xu, "Reduced switching-frequency modulation and circulating current suppression for modular multilevel converters," *IEEE Transactions on Power Delivery*, vol. 26, no. 3, pp. 2009–2017, 2011
- [25] Q. Tu, Z. Xu, Y. Chang, and L. Guan, "Suppressing dc voltage ripples of mmc-hvdc under unbalanced grid conditions," *IEEE Transactions on Power Delivery*, vol. 27, no. 3, pp. 1332–1338, 2012.
- [26] H. Wu, X. Wang, L. Kocewiak, and L. Harnefors, "Ac impedance modeling of modular multilevel converters and two-level voltage-source converters: Similarities and differences," in 2018 IEEE 19th Workshop on Control and Modeling for Power Electronics (COMPEL), 2018, pp. 1–8.
- [27] L. Bessegato, L. Harnefors, K. Ilves, and S. Norrga, "A method for the calculation of the ac-side admittance of a modular multilevel converter," *IEEE Transactions on Power Electronics*, vol. 34, no. 5, pp. 4161–4172, 2019.
- [28] J. Lyu, X. Cai, M. Amin, and M. Molinas, "Subsynchronous oscillation mechanism and its suppression in mmc-based hvdc connected wind farms," *IET Generation, Transmission & Distribution*, vol. 12, 10 2017.
- [29] J. Lyu, X. Cai, and M. Molinas, "Optimal design of controller parameters for improving the stability of mmc-hvdc for wind farm integration," *IEEE Journal of Emerging and Selected Topics in Power Electronics*, vol. 6, no. 1, pp. 40–53, 2018.
- [30] H. Wu, X. Wang, and L. H. Kocewiak, "Impedance-based stability analysis of voltage-controlled mmcs feeding linear ac systems," *IEEE Journal of Emerging and Selected Topics in Power Electronics*, vol. 8, no. 4, pp. 4060–4074, 2020.
- [31] K. Sekiguchi, P. Khamphakdi, M. Hagiwara, and H. Akagi, "A grid-level high-power btb (back-to-back) system using modular multilevel cascade converters without common dc-link capacitor," *IEEE Transactions on Industry Applications*, vol. 50, no. 4, pp. 2648–2659, 2014.
- [32] S. Cui, S. Kim, J.-J. Jung, and S.-K. Sul, "A comprehensive cell capacitor energy control strategy of a modular multilevel converter (mmc) without a stiff dc bus voltage source," in 2014 IEEE Applied Power Electronics Conference and Exposition - APEC 2014, 2014, pp. 602–609.
- [33] S. Cui, H.-J. Lee, J.-J. Jung, Y. Lee, and S.-K. Sul, "A comprehensive acside single-line-to-ground fault ride through strategy of an mmc-based hvdc system," *IEEE Journal of Emerging and Selected Topics in Power Electronics*, vol. 6, no. 3, pp. 1021–1031, 2018.
- [34] L. Bessegato, K. Ilves, L. Harnefors, and S. Norrga, "Effects of control on the ac-side admittance of a modular multilevel converter," *IEEE Transactions on Power Electronics*, vol. 34, no. 8, pp. 7206–7220, 2019.
- [35] H. Shim and N. H. Jo, "An almost necessary and sufficient condition for robust stability of closed-loop systems with disturbance observer,"

- Automatica, vol. 45, no. 1, pp. 296–299, 2009. [Online]. Available: https://www.sciencedirect.com/science/article/pii/S0005109808003749
- [36] H. Shim, Disturbance Observers. Springer London, 2020, p. 1–8. [Online]. Available: http://dx.doi.org/10.1007/978-1-4471-5102-9_100068-1
- [37] M. A. Pérez and J. Rodríguez, "Generalized modeling and simulation of a modular multilevel converter," in 2011 IEEE International Symposium on Industrial Electronics, 2011, pp. 1863–1868.
- [38] R. Lizana, C. Castillo, M. A. Perez, and J. Rodriguez, "Capacitor voltage balance of mmc converters in bidirectional power flow operation," in IECON 2012 - 38th Annual Conference on IEEE Industrial Electronics Society, 2012, pp. 4935–4940.
- [39] G. Buticchi and E. Lorenzani, "Detection method of the dc bias in distribution power transformers," *IEEE Transactions on Industrial Electronics*, vol. 60, no. 8, pp. 3539–3549, 2013.